Supplementary

Effects of SiO_2-Doping on High-Surface-Area Ru/TiO_2 Catalysts for Selective CO Methanation

Sebastian Cisneros,[1‡] Shilong Chen,[1‡] Thomas Diemant,[1] Joachim Bansmann,[1] Ali M. Abdel-Mageed,[1] Michael Goepel,[2] Sine E. Olesen,[3] Eike S. Welter,[2] Magdalena Parlinska-Wojtan,[4] Roger Gläser,[2] Ib Chorkendorff,[3] R. Jürgen Behm*[1]*

[1]Institute of Surface Chemistry and Catalysis, Ulm University, D-89069 Ulm, Germany
[2]Institute of Chemical Technology, Leipzig University, D-04103 Leipzig, Germany
[3]Department of Physics, Technical University of Denmark, DK-2800 Lyngby, Denmark
[4]Institute of Nuclear Physics, Polish Academy of Sciences, Krakow 31-342, Poland

---

[‡] These authors contributed equally.
* Corresponding authors, email: ali.abdel-mageed@uni-ulm.de, juergen.behm@uni-ulm.de

Table of Contents:

1. Experimental

1.1 *UV-Vis spectroscopy (band gap) measurements*

UV/Vis diffuse reflectance spectra were measured using a Lambda 650S UV/Vis spectrophotometer (Perkin Elmer), equipped with an integration sphere (150 mm). The spectra were recorded from 250 to 800 nm with a step width of 1 nm and a slit width of 2 nm. As a reference we used a Spectralon® standard (Labsphere). For the measurements the samples were diluted with $BaSO_4$ (white standard DIN 5033, Merck), resulting in a mixture of 90 wt.% $BaSO_4$ and 10 wt.% sample. The band gap was determined via the theory of Kubelka-Munk, where the experimentally measured reflection R was converted to the remission *F(R)* using eq. (1).

$$F(R) = \frac{(1-R)}{2R} = \frac{k}{s} \tag{1}$$

The band gap was then determined graphically from a plot of F(R) against energy (h(ν)), with the intersection of the linear fit of the slope with the x-axis corresponding to the energy of the band gap.

The error for the determination of the band gap was assumed to be ±0.01 eV. This error was obtained from five consecutive band gap determinations of separately prepared P25 samples. Commercially available P25 (Sigma-Aldrich, 99.5%) was used for these measurements.

1.2 *Operando X-ray Absorption Spectroscopy (XAS) measurements*

Operando X-ray absorption measurements were performed at the P65 applied XAFS beamline of Petra III (DESY, Hamburg) and at the XAFS beamline (Elettra Synchrotrone, Trieste) under continuous flow of reaction gases. At the P65 beamline, we used the continuous XAS mode, which recorded approx. 7500 data points in 3 min between 21 973 eV to 23 122 eV, using a Si(311) crystal monochromator. At the XAFS beamline, Ru-K edge XAS spectra were recorded in the pre-edge region, the near-edge region (XANES) and in the extended-edge region (EXAFS) in transmission mode, using a Si(311) double crystal monochromator. The pre-edge region was scanned from 21 917 to 22 087 (step size 5 eV), the XANES region in the range 22 087 - 22 147 eV (step size 0.4 eV), and the EXAFS region in the range 22 147 – 22 760 eV (step size 0.03 k). The acquisition of the XANES spectra took approximately 5 min per spectrum, EXAFS measurements required around 37 min per spectrum. A Ru foil as well as pellet samples of RuO_2 (Sigma Aldrich, 99.9% purity) and $RuCl_3$ ($RuCl_3$ hydrate, Sigma Aldrich, 99.99%), all measured in transmission mode, were used as reference materials for data evaluation. Background removal and spectra normalization as well as the linear combination analysis (LCA) of the XANES spectra were performed using the Athena software from the IFEFFIT package [1]. For EXAFS evaluation 3 EXAFS spectra were averaged to improve the statistics. The data reduction and subsequent fits of the EXAFS data were performed using the XADP software package with standard procedures, as described elsewhere [2]. Assuming a hcp structure for Ru, theoretical references were calculated by the FEFF 8.0 code and calibrated with measured data of the experimental references (Ru foil, RuO_2, $RuCl_3$) [3,4]. The EXAFS data were evaluated in the R-space (R: 0.0 – 5 Å), using the k-range from 3.2 to 11.2 $Å^{-1}$. In the EXAFS data fit, we allowed the coordination number (CN), the Debye-Waller factor (DWF), the Ru-Ru bond length (R) and the energy shift E_o to change freely.

Measurements were carried out during selective CO methanation in SR-ref 6000 reaction gas mixture at 190 °C after 300 min on stream. Typically, ca. 20 mg of pure catalyst powder were packed in a specially designed cell, which has been described in detail earlier [5]. The effluent gases were analyzed by online infrared spectrometry to follow the CO methanation activity simultaneously with the XAS measurements. For these measurements we used a Bruker Alpha FTIR spectrometer (Bruker Optics Inc., Ettlingen, Germany), which was coupled with a substrate-integrated hollow wave guide (iHWG) for enhanced sensitivity [6].

1.3 *Scanning Transmission Electron Microscopy (STEM) measurements*

The STEM and EDS measurements were performed on a Talos F200 FEI STEM microscope operated at 200 keV in high angle annular dark field conditions (STEM-HAADF). The instrument is equipped with a FEG cathode and the Super EDS system.

1.4 *Pyrrole and pyridine surface titration measurements*

Pyrrole adsorption: The amount of adsorbed pyrrole was determined by DRIFTS. Around 70 mg of the diluted catalyst (1:6 with α-Al_2O_3) were deposited on a 100 mg α-Al_2O_3 layer. After the pre-treatment and activation described with the activity measurements, the catalyst was operated in SR-ref 6000 gas reformate at 190 ºC for 1000 min. Afterwards, the spent catalyst was purged with N_2 at 190 ºC for 1000 min, and subsequently cooled down in N_2 to 30 ºC. Pyrrole vapor with a concentration of 0.23 Vol.% (purity $\geq$ 97.7 % − Merck) was introduced into the DRIFTS cell for 1 h at 30 °C, by bubbling 30 Nml min^{-1} of N_2 (purity > 99.99 %) through a flask containing liquid pyrrole kept at 6°C. Then the cell was purged with N_2 (41.6 Nml min^{-1}) at room temperature for 10 min to remove gas phase and weakly adsorbed pyrrole. Subsequently, the temperature was ramped from 30 ºC to 450 ºC at 10 °C/min in a flow of N_2 (41.6 Nml min^{-1}) for the temperature programmed desorption (TPD) measurement. Once 450 ºC was reached, the temperature was kept constant for 15 min to ensure complete desorption of pyrrole. Pyrrole desorption was followed by monitoring the pyrrole gas phase signal (3567 to 3488 cm^{-1}) by IR transmission spectroscopy. For these measurements we also used a Bruker Alpha FTIR spectrometer (Bruker Optics Inc., Ettlingen, Germany), coupled with a substrate-integrated hollow wave guide (iHWG) [6]. During the measurement the sample compartment of the spectrometer containing the iHWG cell was continuously purged with pure N_2 to ensure a constant background signal within the IR beam path outside the iHWG cell. All IR spectra were recorded in the spectral range 400 -

4000 cm^{-1}, averaging 40 scans for each spectrum during the measurement and 100 scans for the background spectrum. To remove contributions from pyrrole adsorption on the reactor walls, we determined the desorption from an α-Al_2O_3 bed after a similar adsorption procedure and subtracted this from the desorption rates measured for the different catalysts. The total amount of desorbed pyrrole was determined by integration of the pyrrole pressure-time profiles. The IR signal was calibrated before by flowing 30 Nml min^{-1} of N_2 through pyrrole at 6 ºC for 1 hour and correlating the corresponding average peak area in the region 3567 to 3488 cm^{-1} to the known saturation concentration of pyrrole (0.23 Vol.%) under these conditions. Desorption rates were calculated from the pyrrole content in the N_2 stream, as shown in eq. (2),

$$r_{des} = \frac{\dot{n}_{pyrrole}}{m_{catalyst}} \tag{2}$$

where $\dot{n}_{pyrrole}$ is the molar flow rate of desorbed pyrrole.

From the total amount of desorbed pyrrole $n_{pyrrole}$ (in mol g_{cat}^{-1}) we determined the pyrrole coverage $\theta_{pyrrole}$ in ML by equation eq. (3),

$$\theta_{pyrrole} = \frac{\left(\frac{n_{pyrrole} * N_A}{SSA_{catalyst}}\right)}{1.15 * 10^{15}} \tag{3}$$

where N_A is the Avogadro's number and SSA is the specific surface area of the catalyst, as determined by N_2 adsorption. Furthermore, we assume that at most one pyrrole molecule can adsorb per basic site, and a surface density of 1.15×10^{15} cm^{-2} sites.

Pyridine titration: Following similar steps as those for pyrrole adsorption, the DRIFTS cell was purged for 1 h with dilute pyridine vapor in N_2 (concentration 0.43 Vol.%, purity $\geq$ 99.9% -Merck) at 30 °C, by bubbling 30 Nml min^{-1} of N_2 (purity > 99.99 %) for 1 h through a flask containing liquid pyridine, which was kept at 0 °C. Afterwards, the cell was purged with N_2 (41.6 Nml min^{-1}) at room temperature for 10 min to remove gas phase and weakly adsorbed pyridine. The desorption of pyridine was monitored by following the time resolved gas phase signal of pyridine (3130 to 2963 cm^{-1}) in the gas stream, using IR transmission spectroscopy. To remove contributions from pyridine adsorption on the reactor walls, we determined the desorption from an α-Al_2O_3 bed after a similar adsorption procedure and subtracted this from the desorption rates measured for the different catalysts. The total amount of desorbed pyridine was estimated by integration of the pyridine pressure-time profiles. The IR signal was calibrated before by flowing 30 Nml min^{-1} of N_2 through pyridine at 0 ºC for 1 h and correlating the corresponding average peak area in the region 3130 to 2963 cm^{-1} to the known saturation concentration (0.44 vol.%) under these conditions. The corresponding pyridine desorption rates were calculated in a similar way as those for pyrrole.

2. XRD diffractograms of the Ru/TiO_2 catalysts

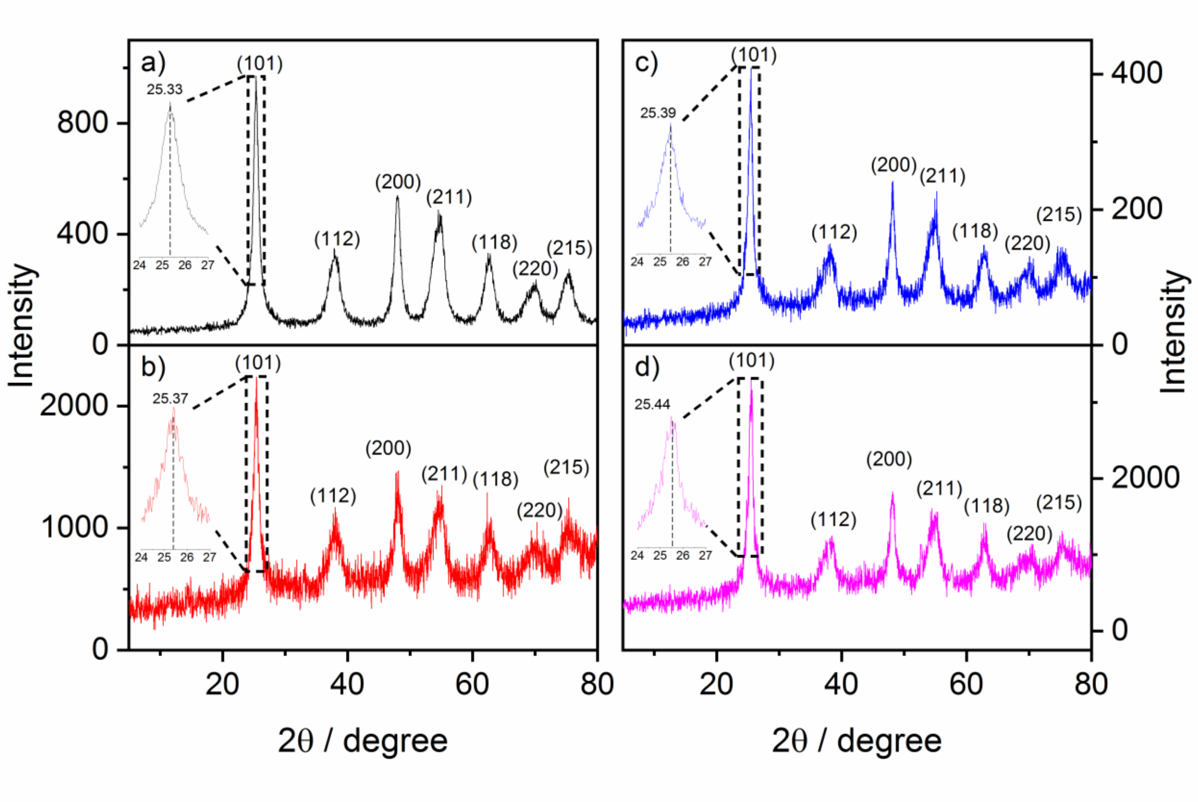

Fig. S1 X-ray diffraction patterns of Ru/TiO_2 catalysts with different Si concentration, wt%: a) Ru/TiO_2 Si; b) Ru/TiO_2 4%Si; c) Ru/TiO_2 8%Si; d) Ru/TiO_2 12%Si. The inset represents a zoom in the respective 101 plane reflection.

We estimated the TiO_2 crystallite sizes from the XRD diffractograms using the Scherrer equation, eq. (4), with $K = 0.89$ and $\lambda = 1.541$ Å. FWHM is the full width at half maximum of the diffraction peak of interest and θ is the angle at which the diffraction signal appears. The sharp and well-defined reflection lines in the diffractogram indicate crystalline TiO_2 supports. The marked lines are assigned to the different planes of anatase, while the signals corresponding to the rutile phase are almost undetectable. That is, the diffractograms reveal a clear predominance of the anatase phase for all support materials.

$$D = \frac{K\lambda}{FWHM \times \cos(\theta)} \tag{4}$$

Table S1: Structural parameters of TiO_2 determined from the main reflection (A(101)) of each catalyst after 1000 min reaction

Parameter	Ru/TiO_2	Ru/TiO_2-4	Ru/TiO_2-8	Ru/TiO_2-12
SSA / m^2g^{-1}	225 ± 18	266 ± 21	250 ± 20	270 ± 22
TiO_2 crystallite size D / nm	6.9 ± 0.9	6.6 ± 0.6	7.3 ± 0.7	8.1 ± 0.3
θ / º	25.33±0.03	25.37±0.03	25.39±0.03	25.44±0.04
FWHM	1.15±0.03	1.22±0.03	1.12±0.03	1.09±0.03

3. CO methanation on Ru/TiO_2 catalysts at 190 ˚C

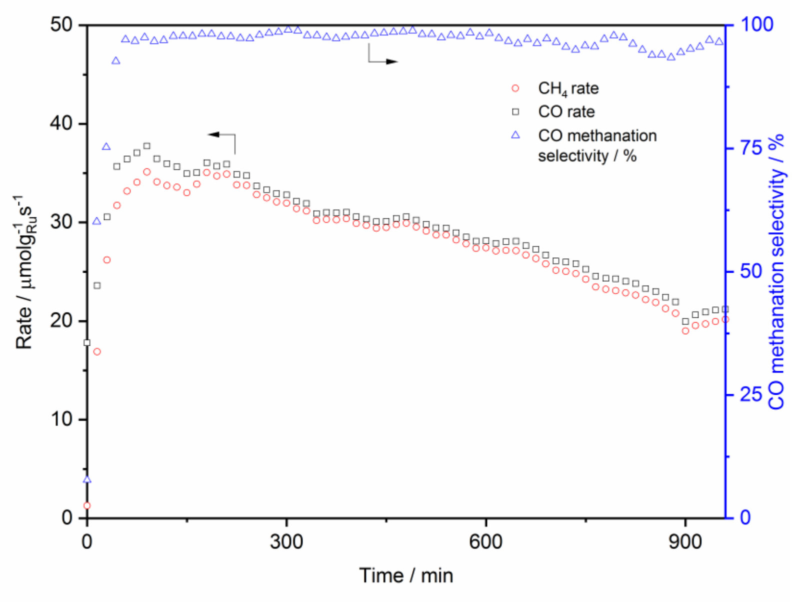

Fig. S2 Temporal evolution of the CO consumption reaction rate, methane formation rate and the selectivity for methane formation on Ru/TiO_2-4 in SR-ref100.

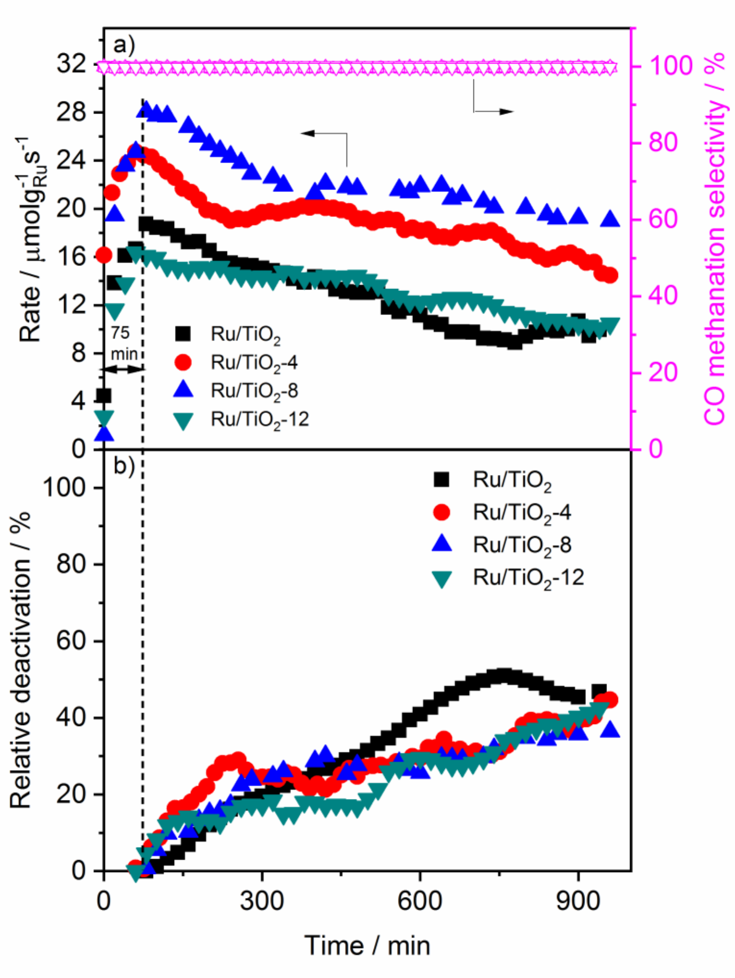

Fig. S3 a) Temporal evolution of the CO consumption rate, and selectivity for methane formation from CO rather than from CO_2 methanation; b) relative deactivation with time on stream (see eq. (8)) in SR-ref-W 6000.

4. (S)TEM images of the Si-doped Ru/TiO_2 catalysts

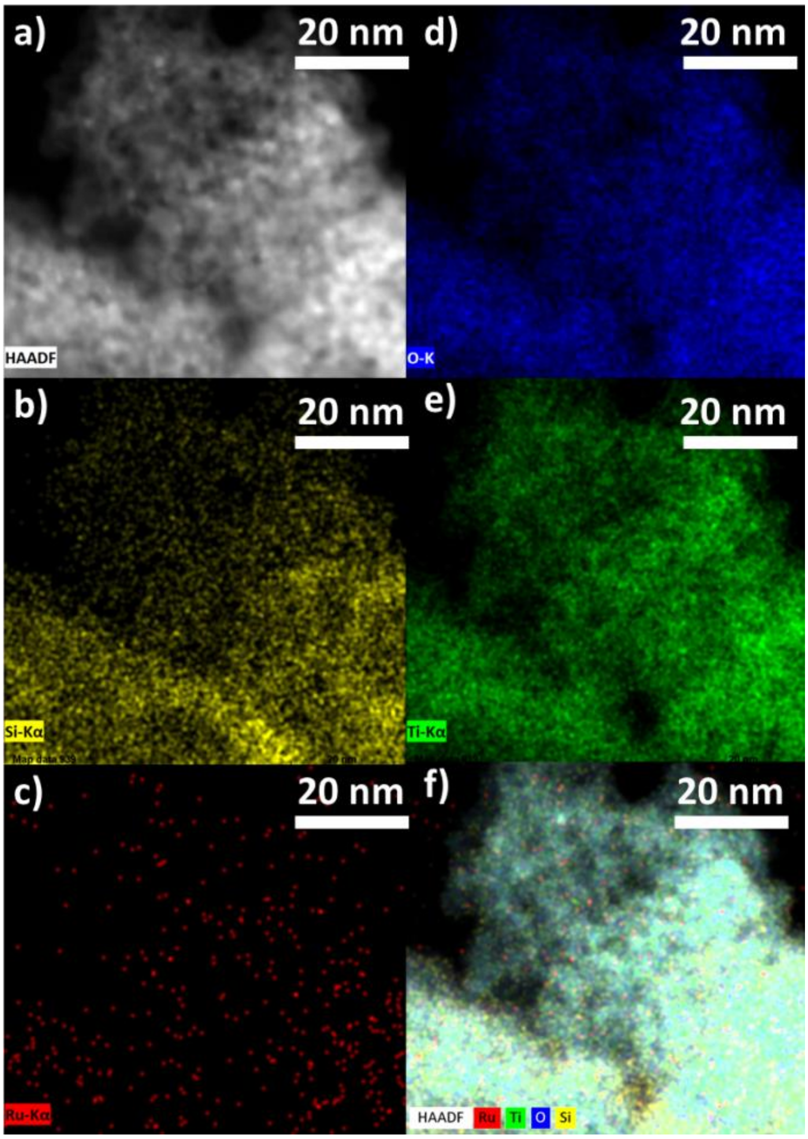

Fig. S4 HAADF-EDS maps of the elemental distribution on the surface of the Ru/TiO_2-4 catalyst after reaction in SR-ref 6000 at 190 °C. a) HAADF image, b) Si, c) Ru, d) O, e) Ti, f) complete map (yellow: Si, red: Ru, blue: O, green: Ti).

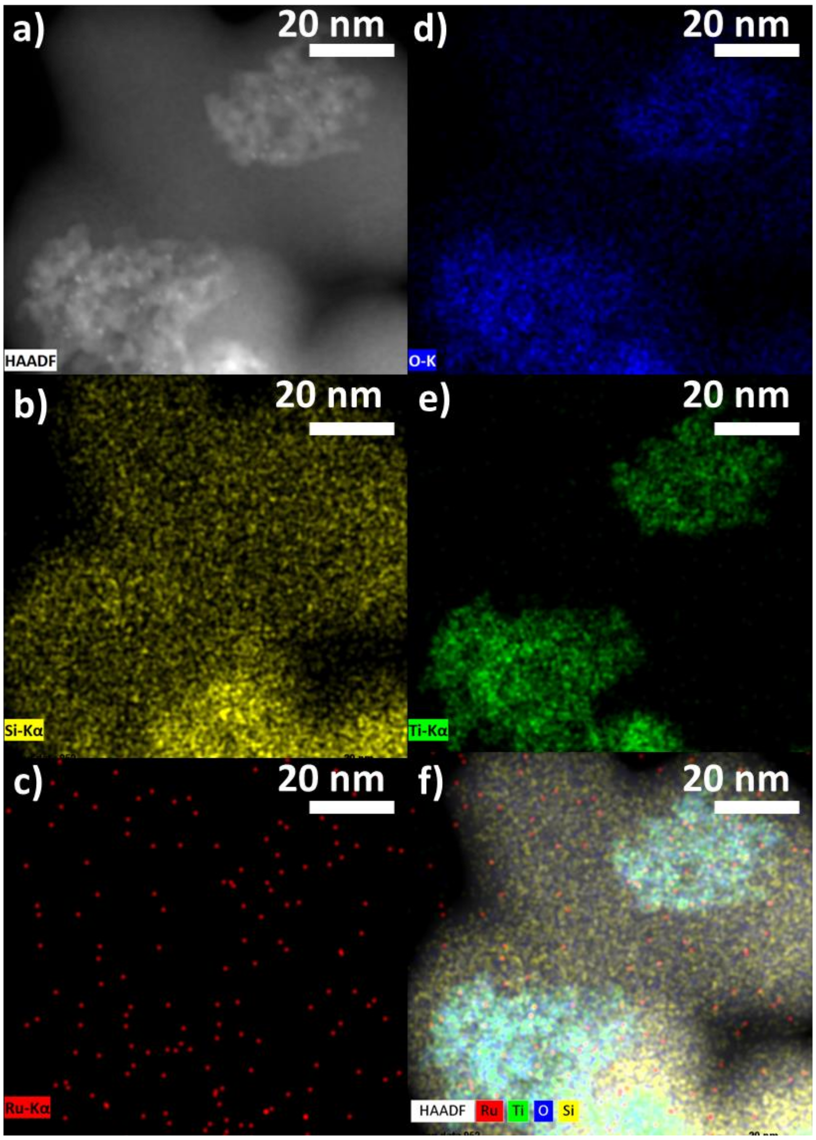

Fig. S5 HAADF-EDS maps of the elemental distribution on the catalyst surface after reaction in SR-ref 6000 at 190 °C on the Ru/TiO_2-8 catalyst. a) HAADF image; b) Si, c) Ru, d) O, e) Ti, f) complete map (yellow: Si, red: Ru; blue: O, green: Ti).

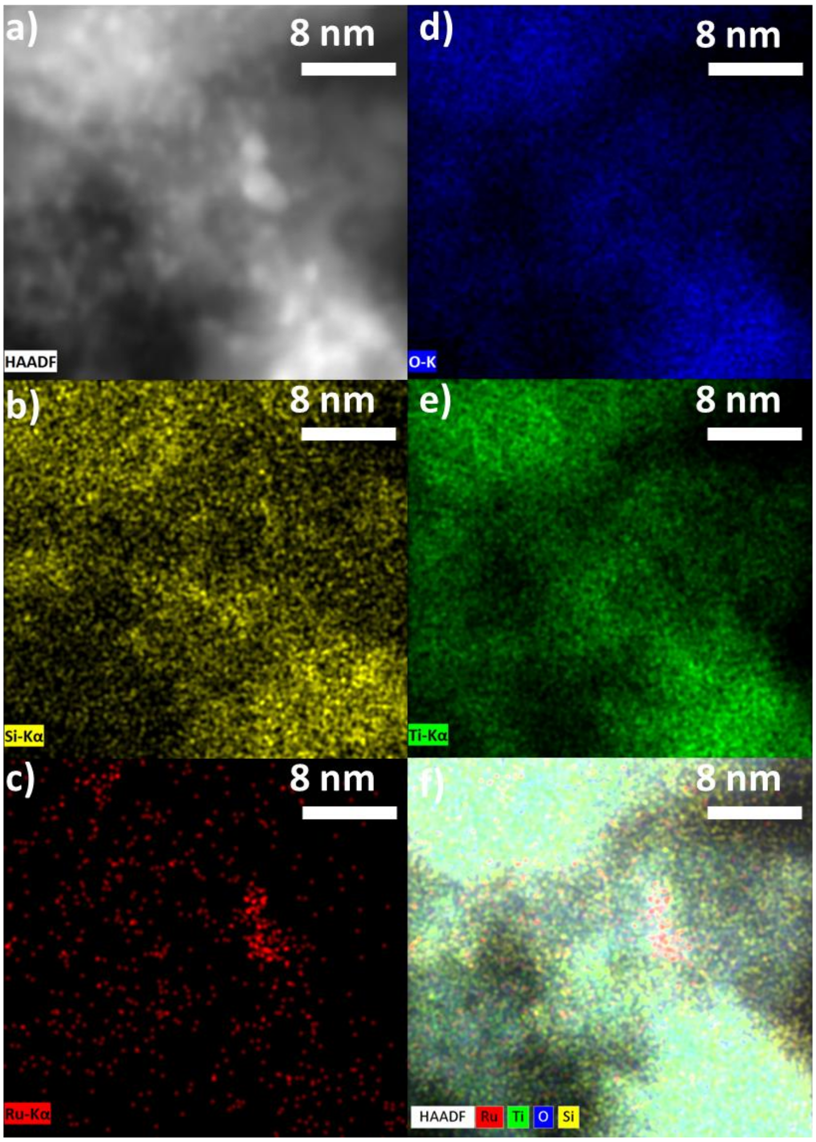

Fig. S6 HAADF-EDS maps of the elemental distribution on the catalyst surface after reaction in SR-ref 6000 at 190 °C on the Ru/TiO_2-12 catalyst. a) HAADF image, b) Si, c) Ru, d) O, e) Ti, f) complete map (yellow: Si, red: Ru, blue: O; green: Ti).

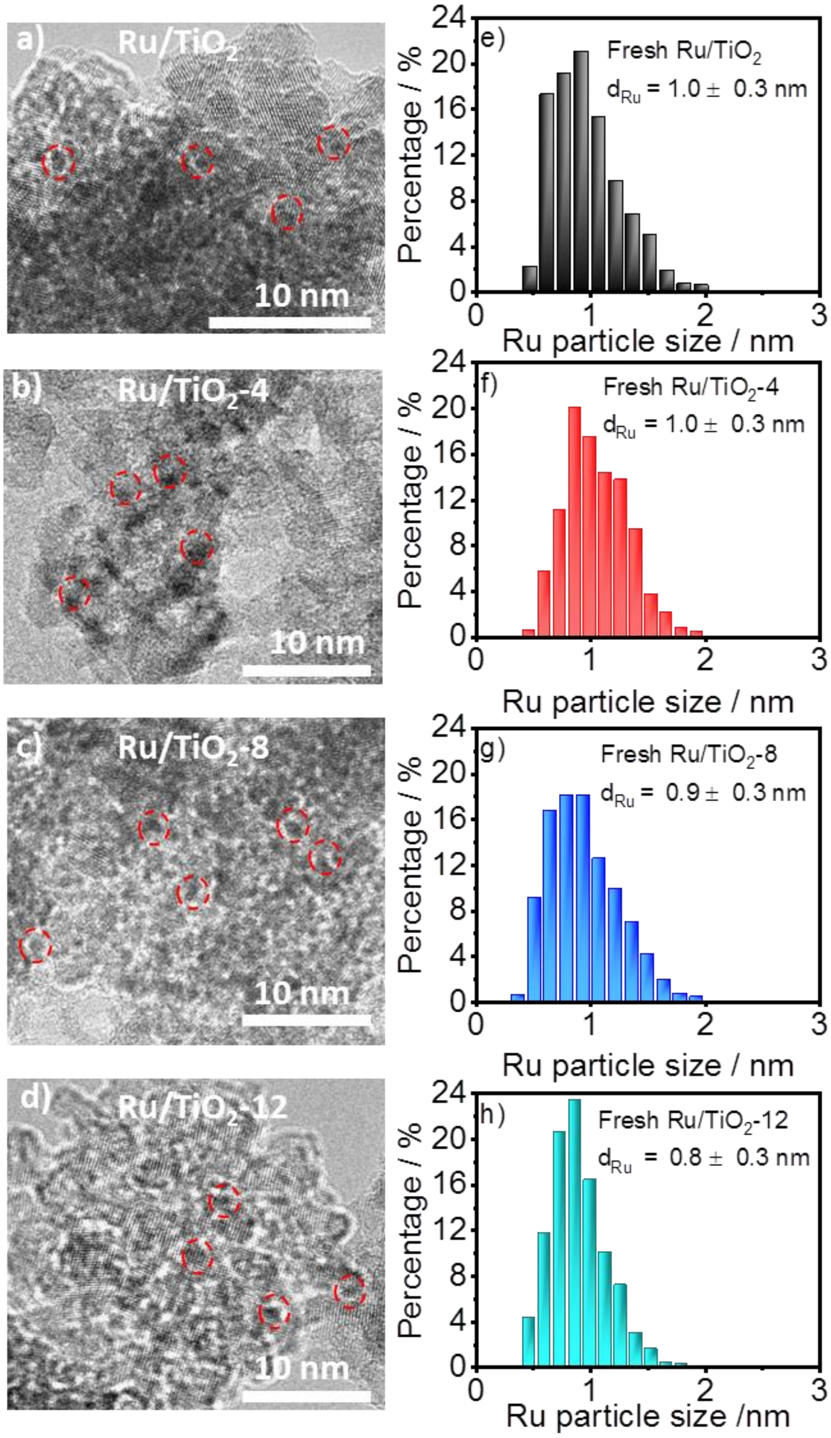

Fig. S7 Representative TEM images of the ‘fresh’ Ru/TiO$_2$ catalysts after 10 min on stream (a-d) and the corresponding Ru particle size distributions (e-h).

5. UV-Vis measurements of the band gap of the different catalysts

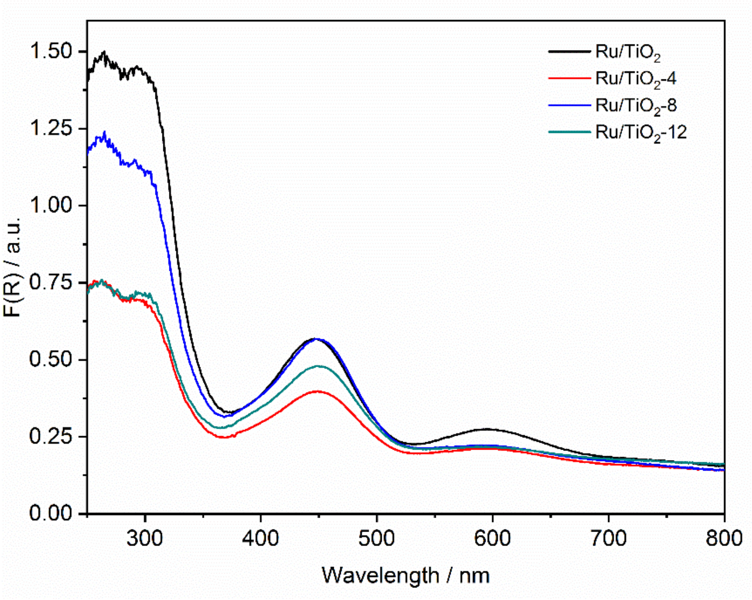

Fig. S8 Remission (F(R)) as a function of wavelength of the different fresh catalysts (a) Ru/TiO$_2$, b) Ru/TiO$_2$-4, c) Ru/TiO$_2$-8 and d) Ru/TiO$_2$-12) in the UV-vis measurements.

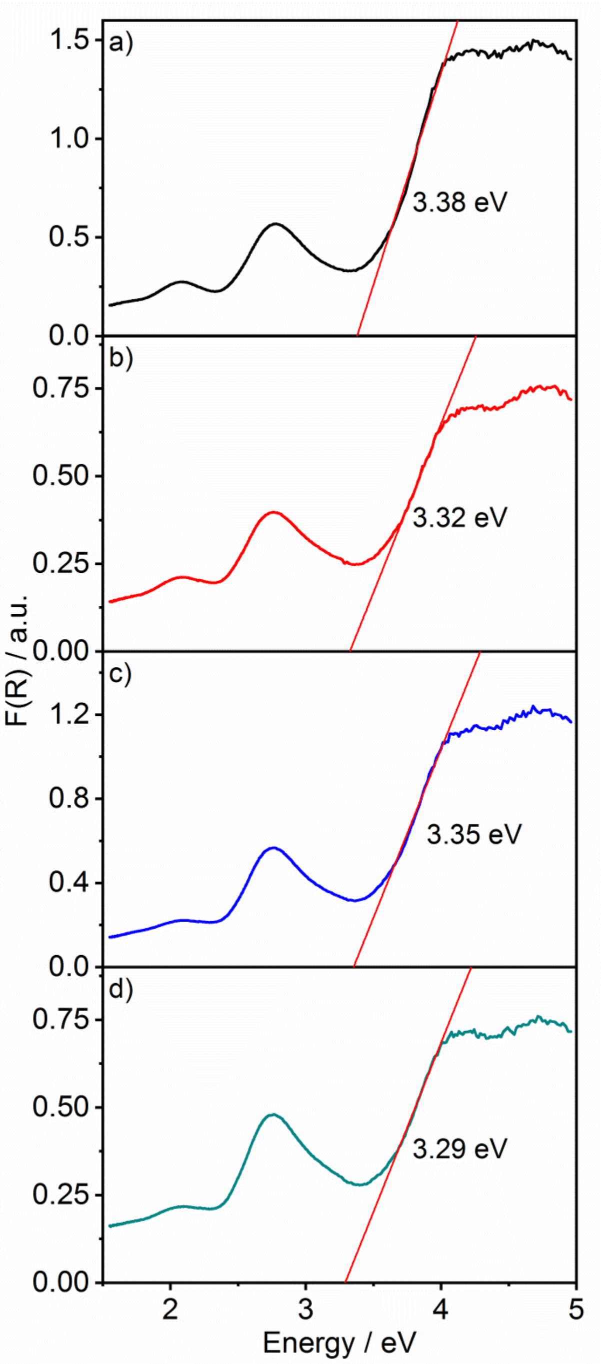

Fig. S9 Band gap energies derived from UV-Vis measurements, based on the Kubelka-Munk-theory for a) the Ru/TiO_2, b) Ru/TiO_2-4, c) Ru/TiO_2-8 and d) Ru/TiO_2-12 fresh catalyst.

6. *Operando* EXAFS measurements of the different catalysts during reaction

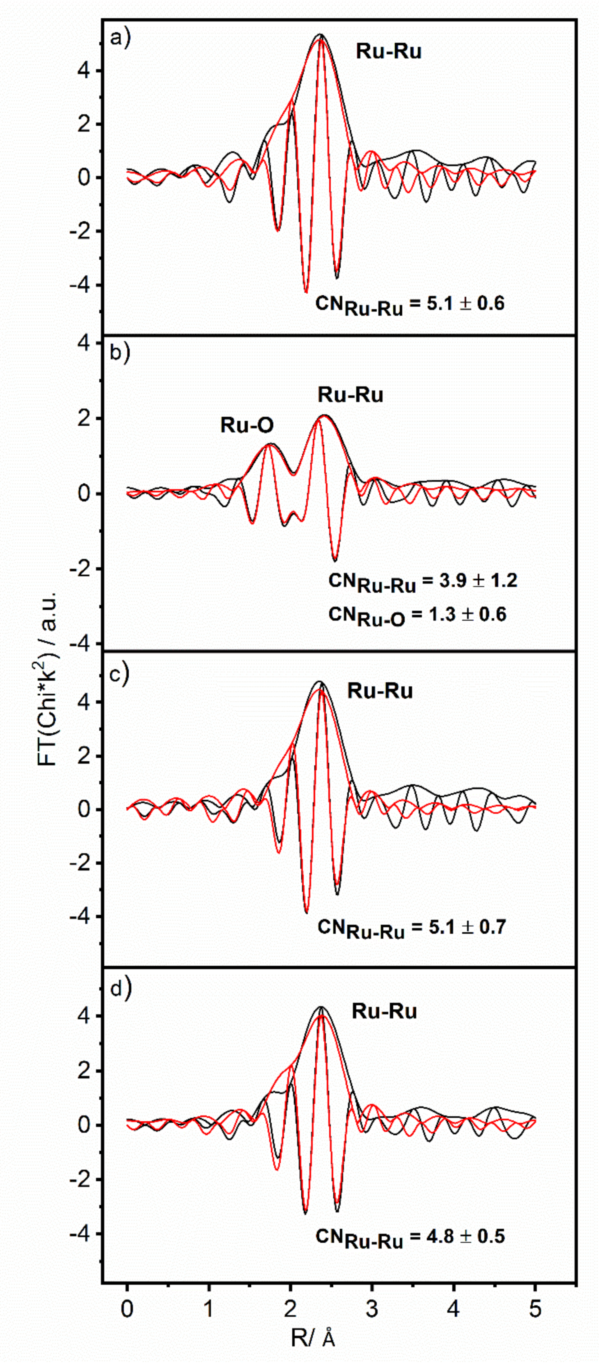

Fig. S10 Fourier transformed EXAFS spectra collected at the Ru K-edge during reaction (300 min on stream) in SR-ref 6000 on a) Ru/TiO_2, b) Ru/TiO_2-4, c) Ru/TiO_2-8, d) Ru/TiO_2-12.

Table S2: Structural parameters extracted from EXAFS spectra collected on the different catalysts during reaction in SR-ref 6000 reformate at 190 °C. For the Ru/TiO2-4 catalyst we also included values for Ru-O backscattering (2^{nd} line)

Catalyst	CN	σ^2 /Å^2	R / Å	E_0 / eV
Ru/TiO_2	5.3 ± 0.6	0.004 ± 0.0016	2.65 ± 0.02	10 ± 1
Ru/TiO_2-4	4.0 ± 1.2 1.3 ± 0.6	0.01 ± 0.006 0 ± 0.007	2.61 ± 0.03 2.22 ± 0.04	7 ± 3 -10 ± 4
Ru/TiO_2-8	5.1 ± 0.7	0.005 ± 0.002	2.66 ± 0.02	10 ± 1
Ru/TiO_2-12	4.8 ± 0.5	0.005 ± 0.002	2.66 ± 0.02	9 ± 1

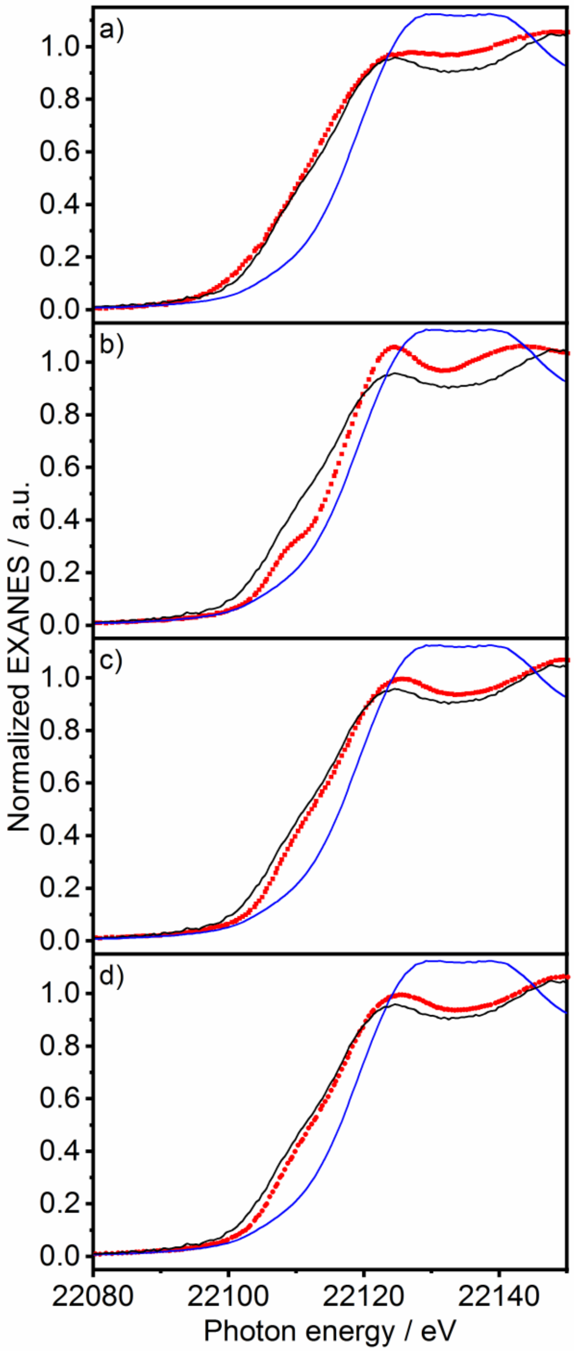

Fig. S11 Linear combination analysis (LCA) of Ru K-edge XANES spectra recorded during reaction in SR-ref 6000 at steady-state on a) Ru/TiO_2, b) Ru/TiO_2-4, c) Ru/TiO_2-8, d) Ru/TiO_2-12. Red dots: original spectra, black lines: fit curves based on Ru foil, blue lines: fit curves based on RuO_2 powder.

7. XP detail spectra

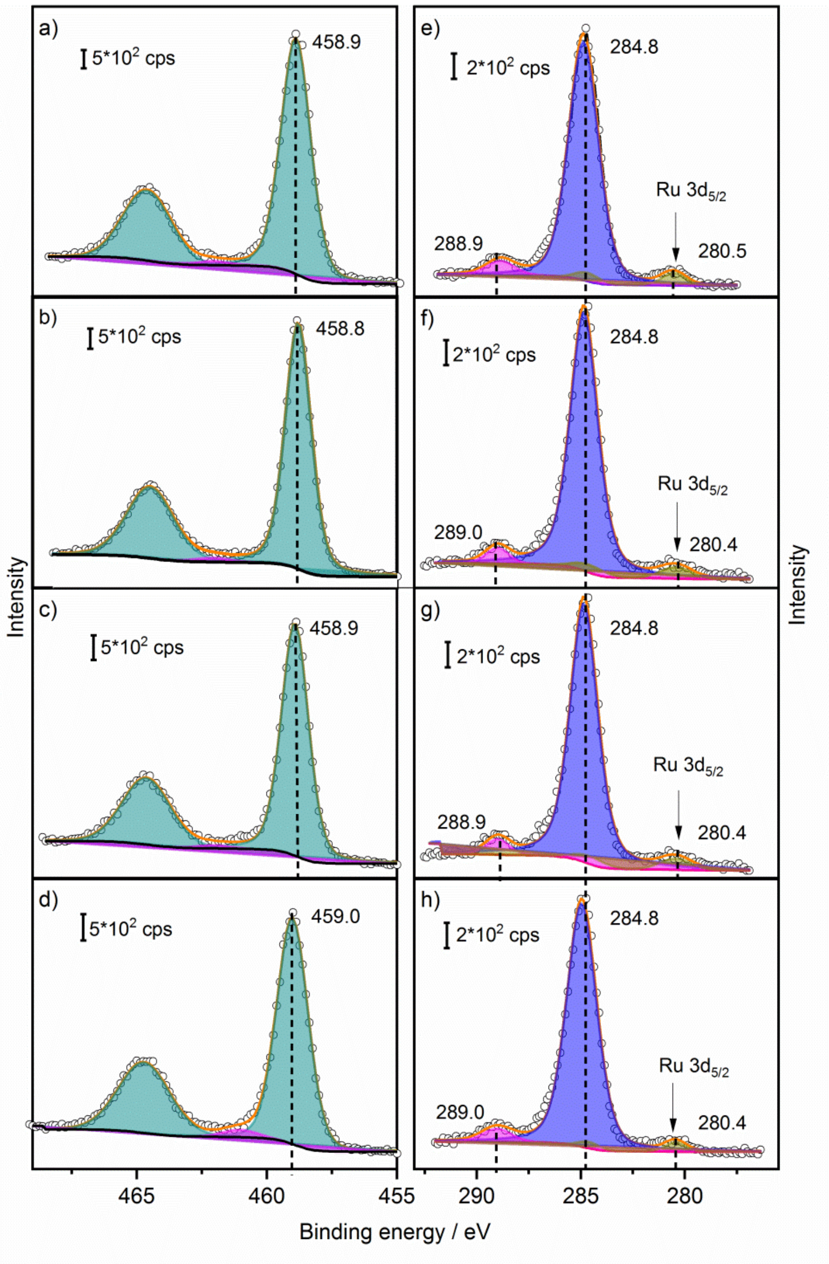

Fig. S12 XPS spectra of the Ti (2p) region (left panel) and of the C(1s) + Ru(3d) region (right panel) of the Ru/TiO_2 catalysts with different Si concentration: a), e) Ru/TiO_2; b), f) Ru/TiO_2-4; c), g) Ru/TiO_2-8; d), h) Ru/TiO_2-12.

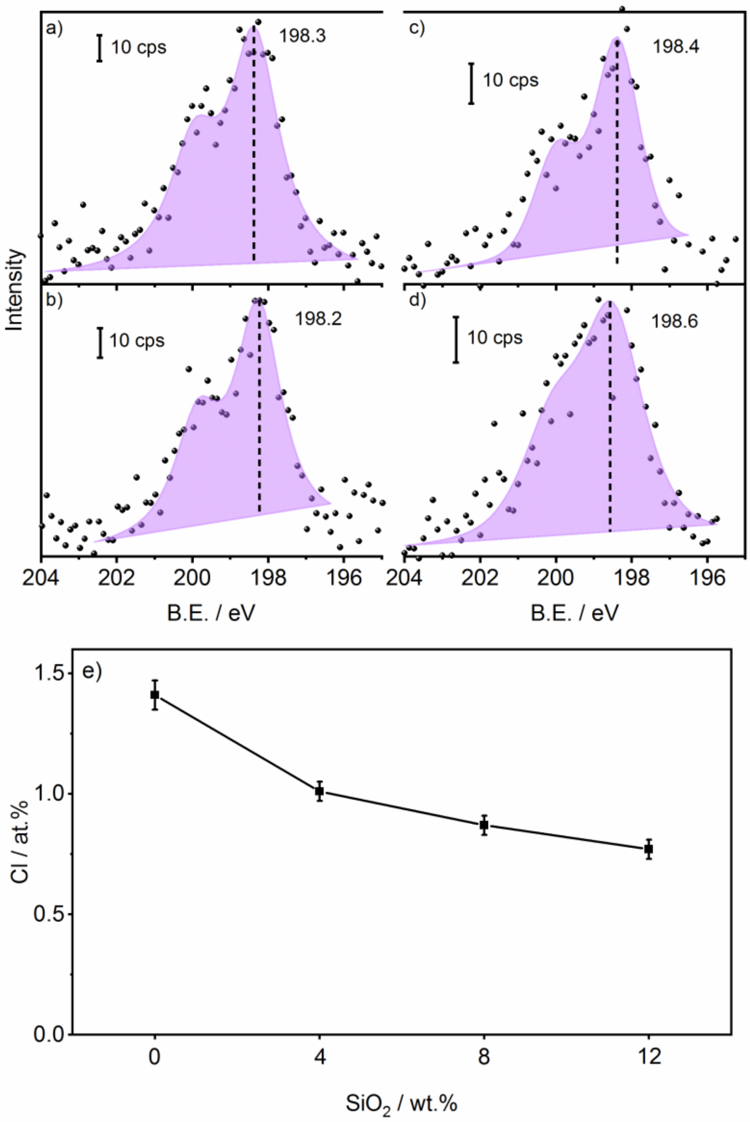

Fig. S13 XP spectra of the Cl (2p) range of the different Ru/TiO$_2$ catalysts (a) Ru/TiO$_2$, b) Ru/TiO$_2$-4, c) Ru/TiO$_2$-8 and d) Ru/TiO$_2$-12); e) surface atomic Cl content as function of Si doping.

Table S3: Binding energies of additional elements as determined by XPS.

Parameter	Ru/TiO_2	Ru/TiO_2-4	Ru/TiO_2-8	Ru/TiO_2-12
O(1s) BE / eV (XPS) (lattice TiO_2)	530.0 ± 0.1	530.0 ± 0.1	530.0 ± 0.1	530.1 ± 0.1
O(1s) BE / eV (XPS) (OH)	530.8± 0.1	530.9± 0.1	530.9± 0.1	531.0± 0.1
O(1s) BE / eV (XPS) (OH) (carboxylates)	532.1± 0.1	531.9± 0.1	532.0± 0.1	532.1± 0.1
O(1s) BE / eV (XPS) (OH) (lattice SiO_2)	--	533.0± 0.1	532.9± 0.1	533.1± 0.1
Cl($2p_{1/2}$) BE / eV (XPS)	198.3± 0.1	198.2± 0.1	198.4± 0.1	198.6± 0.1

8. DRIFT spectra and intensity of CO$_{ad}$ bands during reaction in SR-ref6000

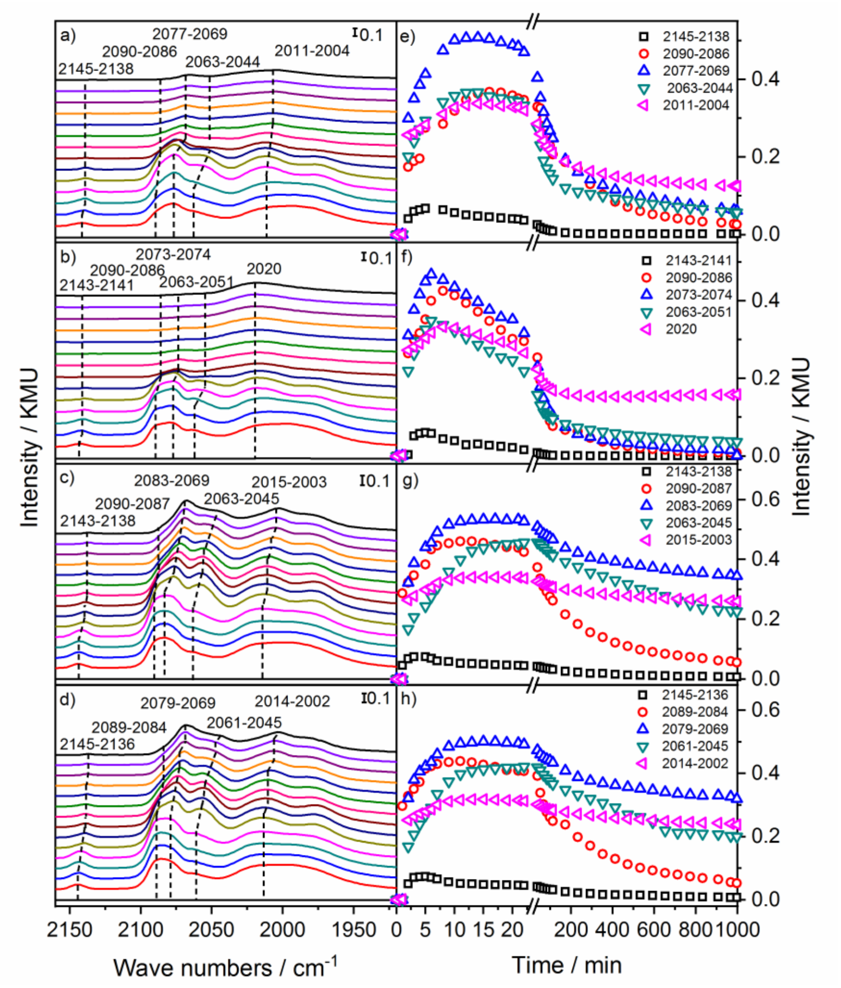

Fig. S14 Left column: DRIFTS spectra recorded during reaction at 190 °C in SR-ref 6000 (0.6 % CO, 3% N_2, balance H_2) on a) Ru/TiO_2; b) Ru/TiO_2-4; c) Ru/TiO_2-8; d) Ru/TiO_2-12 catalysts at different times (from top to bottom:0, 1, 2, 5, 15, 20, 37, 112, 172, 292, 412, 472, 592, 907 and 1000 min, respectively). Right column: Temporal evolution of the KMU intensity of the different CO$_{ad}$ bands on e) Ru/TiO_2-0, f) Ru/TiO_2-4, g) Ru/TiO_2-8, h) Ru/TiO_2-12.

9. DRIFT spectra and intensity of CO_{ad} bands during CO desorption in N_2

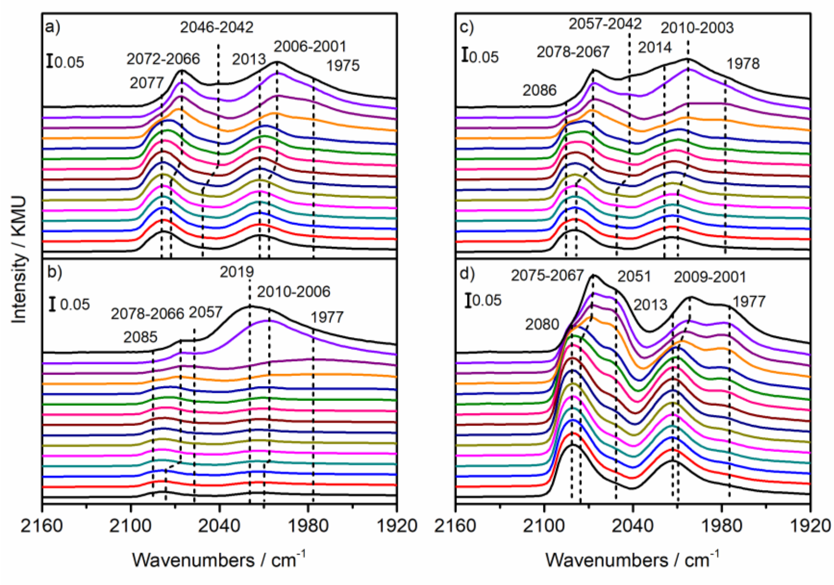

Fig. S15 DRIFTS spectra of the CO range recorded during isothermal desorption in N_2 at 190 °C after CO methanation in CO_2 free atmosphere (ID-ref 6000: 0.6 % CO, 3% N_2, balance H_2) at 190 °C on a) Ru/TiO_2-0; b) Ru/TiO_2-4; c) Ru/TiO_2-8; d) Ru/TiO_2-12 at different times (from top to bottom:0, 1, 2, 5, 15, 20, 37, 112, 172, 292, 412, 472, 592, 907 and 1000 min, respectively).

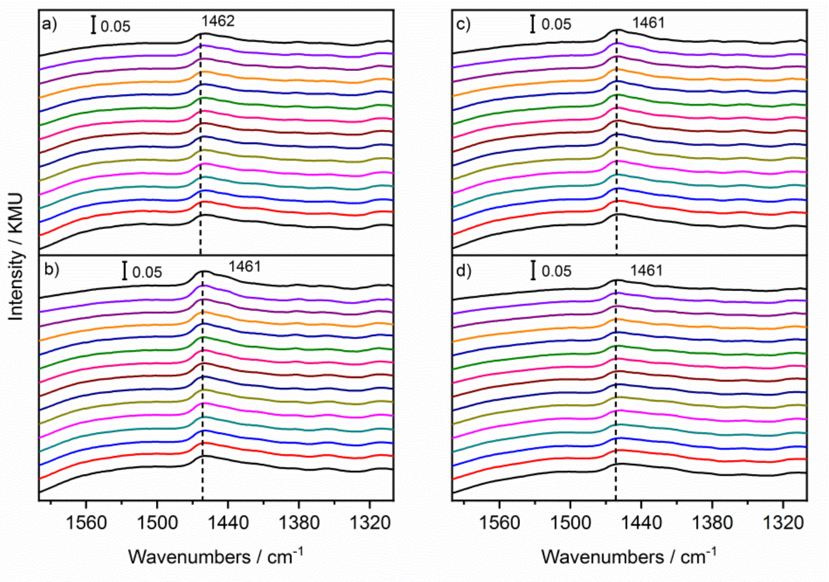

Fig. S16 DRIFTS spectra of the O-C-O region recorded during isothermal desorption in N_2 at 190 °C after CO methanation in CO_2 free atmosphere (ID-ref 6000: 0.6 % CO, 3% N_2, balance H_2) at 190 °C on a) Ru/TiO_2-0; b) Ru/TiO_2-4; c) Ru/TiO_2-8; d) Ru/TiO_2-12 at different times (from top to bottom:0, 1, 2, 5, 15, 20, 37, 112, 172, 292, 412, 472, 592, 907 and 1000 min, respectively).

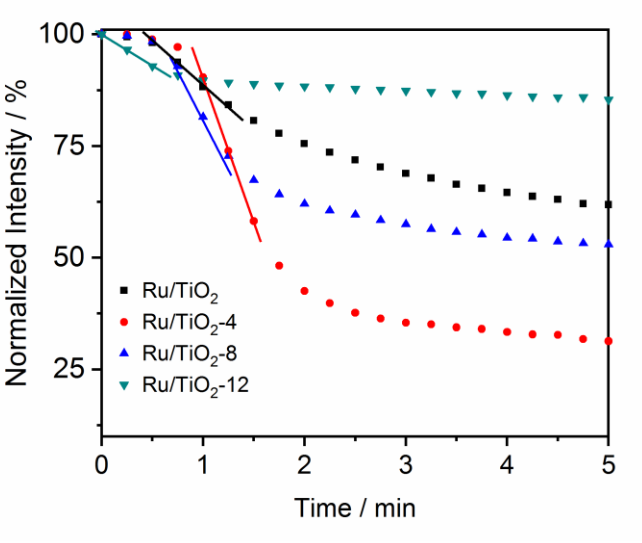

Fig. S17 Time evolution of the relative intensity of the CO_{ad} related bands, normalized to 100 %, during the first 5 min desorption in N_2 at 190℃, after 1000 min reaction in ID-ref 6000 at 190°C. The initial slopes are indicates as lines.

10. Surface titration of basic and acidic sites of TiO_2-SiO_2

For further information on the chemical nature of the support surface we characterized the basic and acid properties of the TiO_2-based supports by titration experiments. The stretch vibration of the N-H bond (ν(N-H) band) of adsorbed pyrrole can be used as a direct probe of the Lewis basic character of a surface, due to the weakening of the N-H bond upon interaction of the H atom with free electrons at sites such as O^{2-} and OH^- sites [7]. Steady-state DRIFT spectra recorded during surface titration with pyrrole are shown in Fig. S18a. The spectra display a broad absorption band in the region 3490 – 3200 cm^{-1}, which indicates the presence of adsorbed pyrrole species, interacting with O^{2-} sites on the oxide surface via the N-H groups [8]. The weaker absorption bands at 3540 and 3518 cm^{-1} are attributed to N-H vibrations of gas phase pyrrole [8], bands at 3138, 3104 and 3057 cm^{-1} are close to the absorption bands associated with C-H stretching of the pyrrole ring in the gas phase [9-11]. The bands at around 3740 and 3670 cm^{-1} finally represent the O-H stretch frequency of isolated surface hydroxyl groups on SiO_2 and on TiO_2 (anatase), respectively [9,12]. Based on the higher intensity of the bands in the range 3490 – 3200 cm^{-1} on the Ru/TiO_2 catalyst, we expect a more pronounced basic character of the adsorption sites on the Ru/TiO_2 catalyst compared to those on the Si doped ones. To obtain more quantitative information about the concentration of basic sites and their adsorption strength we performed TPD measurements. The corresponding IR spectra of the desorbing pyrrole (gas phase spectra) and the resulting desorption rates are shown in Fig, S19 and S20, together with the accumulated amount of desorbed pyrrole. Integration of the total amount of desorbed pyrrole results in the following order in coverage of adsorbed pyrrole on the respective Ru/TiO_2 catalysts: Ru/TiO_2 >> Ru/TiO_2-8 ≈ Ru/TiO_2-4 ≈ Ru/TiO_2-12, where the coverage is relative to the density of surface O^{2-} ions in TiO_2 ($\sim 1.15 \times 10^{-15}$ atoms cm^{-2}) (Fig. S18b). The amount of basic surface sites is roughly 3-fold higher on the Ru/TiO_2 catalysts than on the Si doped Ru/TiO_2 catalysts, while there is no significant difference between the latter ones.

The maximum desorption rate of pyrrole on the Ru/TiO_2 catalyst, used as a measure of the pyrrole adsorption strength, was at a higher temperature (89±5 °C) on the non-doped Ru/TiO_2 catalyst than on the Si-doped catalysts (65±3 °C) (see Fig. S18c). Hence, not only the concentration of basic sites is affected, but also their basicity is affected by Si doping. In these experiments higher Si concentrations, in excess of 4 wt.% SiO_2, do not seem to matter.

Similar type adsorption measurements were performed to test the acidic properties of the catalysts, using pyridine as probe molecule. From the absence of the characteristic absorption bands of pyridinium ions in the range 1500-1550 cm^{-1} and 1630 cm^{-1} (see Fig. S22a) [13-15], we conclude that there are no Brønsted acidic sites on these catalysts. The amount of pyridine adsorbed on Lewis acidic sites, characterized by bands at 1443 and 1579 cm^{-1} [14,15], changed very little with increasing Si doping. In the TPD measurements we found that the desorption rate abruptly increased upon heating and then decayed continuously, distinct desorption peaks were not observed (see Fig. S23 and S24). The absence of a distinct desorption peak indicates that pyridine adsorption is rather weak, activating desorption immediately upon heating. For the saturation coverage we would have expected comparable changes as for pyrrole adsorption, assuming that pyridine adsorption on Si^{4+} cations is sufficiently weak that it does not contribute, and that Ti^{4+} sites are fully covered with adsorbed pyridine. Considering that according to the XPS data the concentration of surface Ti^{4+} sites decreases from 33 % to 26 % (see Table 2, main text) we tentatively explain this observation by either a partial blocking of Ti^{4+} surface sites by contributions of O-C-O groups of species that were adsorbed on the surface before pyridine adsorption and that interfere with the bands of adsorbed pyridine.

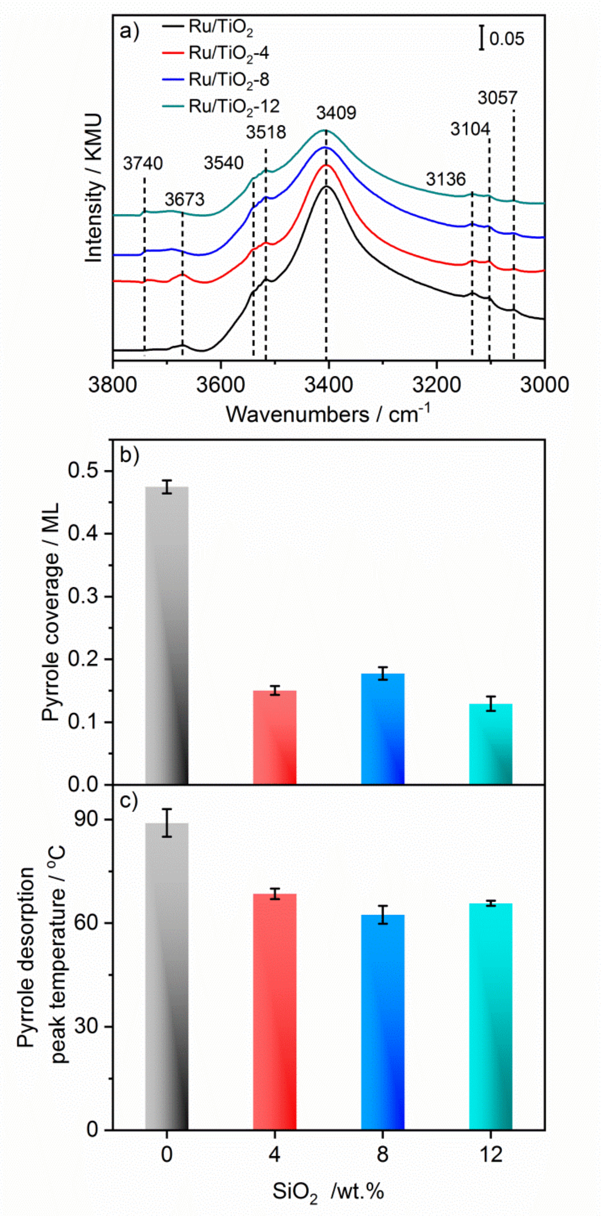

Fig. S18 a) DRIFT spectra of the different Ru/TiO_2 catalysts recorded during pyrrole adsorption (N-H stretching region) at 30°C, after reaction in SR-ref 6000 at 190°C, desorption in N_2 at 190°C and subsequent 60 min of pyrrole adsorption. b) Accumulated catalyst mass-normalized pyrrole desorption during TPD between 30°C and 450°C after background correction; c) temperature at maximum pyrrole desorption rate (black: Ru/TiO_2, red: Ru/TiO_2-4, blue: Ru/TiO_2-8, green: Ru/TiO_2-12).

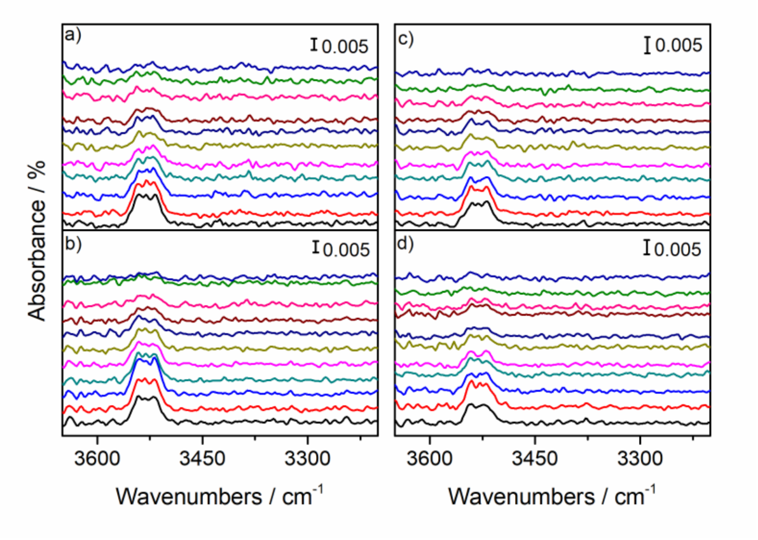

Fig. S19 Pyrrole IR transmission spectra recorded during TPD after reaction in SR-ref 6000 atmosphere at 190 °C, subsequent desorption in N_2, and finally pyrrole adsorption at 30 °C (30 min) on a) Ru/TiO_2; b) Ru/TiO_2 4%Si; c) Ru/TiO_2 8%Si; d) Ru/TiO_2 12%Si at different catalyst temperatures (30 °C, 33 °C, 45 °C, 55 °C, 105 °C,125 °C, 270 °C, 345 °C and 450 °C).

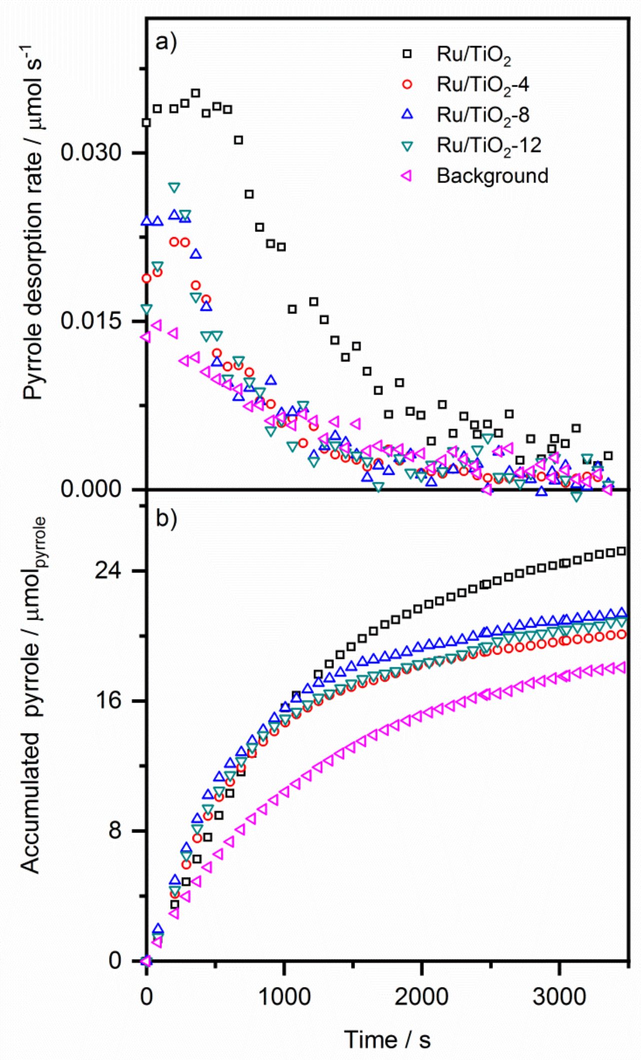

Fig. S20 a) Pyrrole desorption rate and b) pyrrole accumulation on the various catalysts during TPD after reaction in SR-ref 6000 atmosphere at 190 °C.

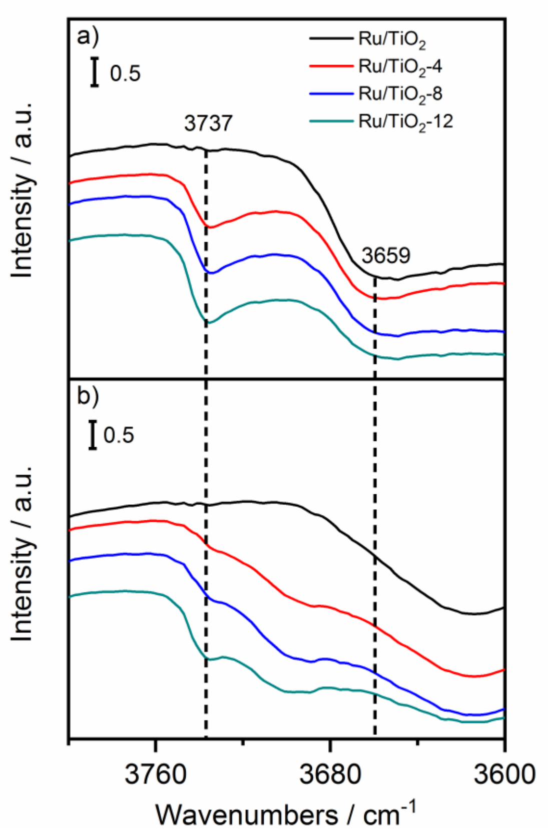

Fig. S21 DRIFT spectra (raw data) of the O-H region recorded on a) the freshly calcined catalysts (before reaction) and on b) the spent catalysts (after 1000 min reaction). The band at ca. 3737 cm^{-1} corresponds to the O-H stretch on Si, the band at ca. 3659 cm^{-1} to that on anatase.

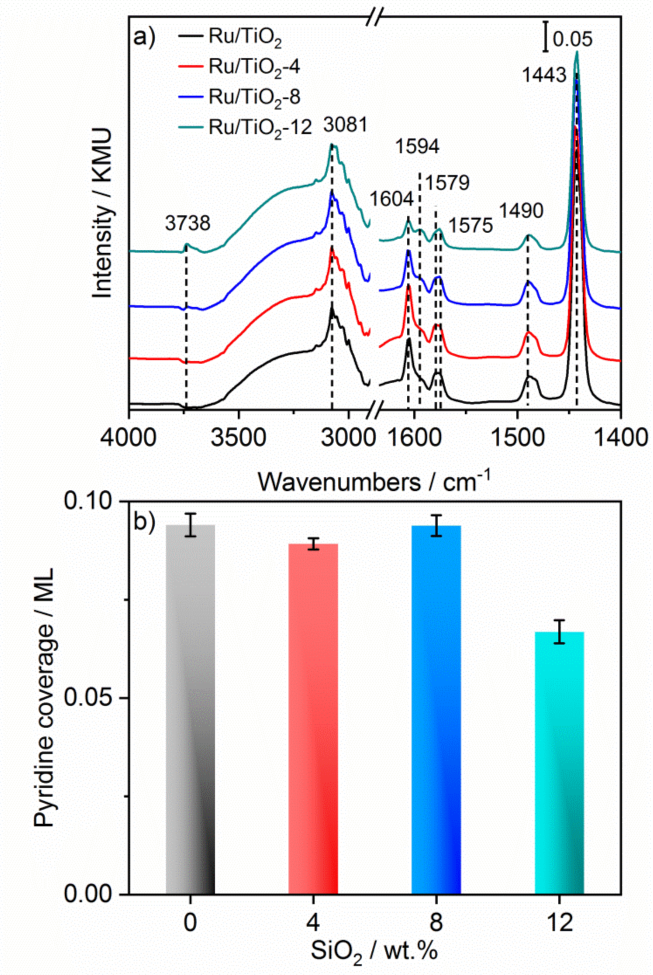

Fig. S22 a) DRIFT spectra of the different Ru/TiO_2 catalysts recorded during pyridine adsorption (pyridine ring vibration region) at 30°C under steady-state conditions, after reaction in SR-ref 6000 at 190°C, desorption in N_2 and subsequent 60 min of pyridine adsorption; b) accumulated catalyst mass-normalized pyridine desorption during TPD between 30°C and 450°C after background correction c) temperature at maximum pyridine desorption rate (black: Ru/TiO_2, red: Ru/TiO_2-4, blue: Ru/TiO_2-8, green: Ru/TiO_2-12).

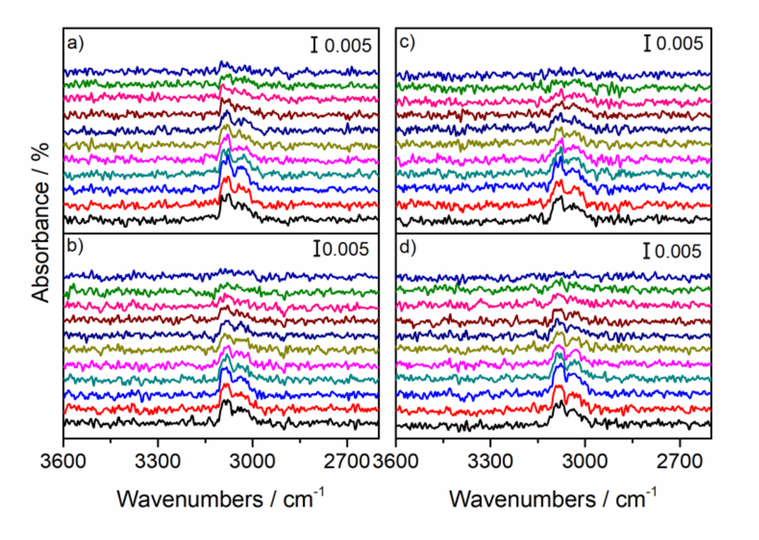

Fig. S23 Pyridine IR transmission spectra recorded during TPD after reaction in SR-ref 6000 atmosphere at 190 °C, subsequent desorption in N_2 (1000 min), and finally pyridine adsorption at 30 °C (30 min) on a) Ru/TiO_2; b) Ru/TiO_2-4; c) Ru/TiO_2-8; d) Ru/TiO_2-12 at different catalyst temperatures (from bottom to top: 30 °C, 33 °C, 45 °C, 55 °C, 105 °C,125 °C, 270 °C, 345 °C and 450 °C).

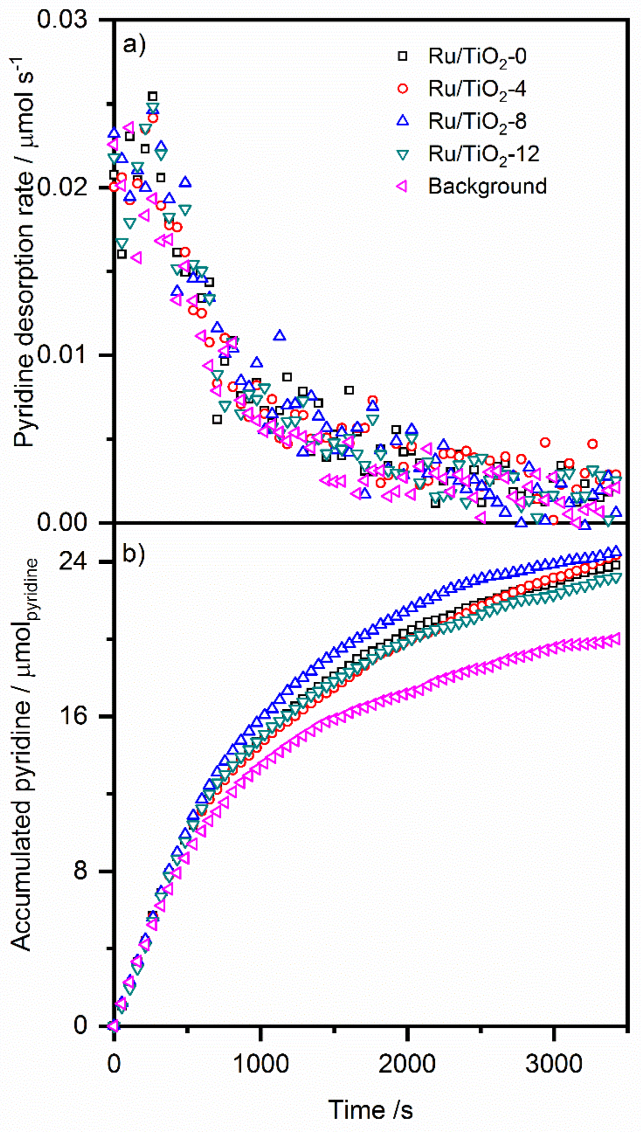

Fig. S24 a) Pyridine desorption rate and b) pyridine accumulation on the various catalysts during TPD after reaction in SR-ref 6000 atmosphere at 190 °C.

11. References

[1] M. Newville, IFEFFIT : Interactive XAFS analysis and FEFF fitting, J. Synchrotron Rad. 8 (2001) 322-324.

[2] M. Vaarkamp, J.C. Linders, D.C. Koningsberger, A new method for parameterization of phase shift and backscattering amplitude, Physica B 208-209 (1995) 159-160.

[3] A.L. Ankudinov, B. Ravel, J.J. Rehr, S.D. Conradson, Real-space multiple-scattering calculation and interpretation of x-ray-absorption near-edge structure, Phys. Rev. B 58 (1998) 7565-7576.

[4] D.C. Koningsberger, B.L. Mojet, G.E. van Dorssen, D.E. Ramaker, XAFS spectroscopy; fundamental principles and data analysis, Top. Catal. 10 (2000) 143-155.

[5] S. Eckle, M. Augustin, H.-G. Anfang, R.J. Behm, Influence of the catalyst loading on the activity and the CO selectivity in the selective methanation of CO in CO_2 containing feed gases over Ru supported catalysts, Catal. Today 181 (2012) 40-51.

[6] V. Kokoric, D. Widmann, M. Wittmann, R.J. Behm, B. Mizaikoff, Infrared spectroscopy via substrate-integrated hollow waveguides: a powerful tool in catalysis research, Analyst 141 (2016) 5990-5995.

[7] J.C. Lavalley, Infrared spectrometric studies of the surface basicity of metal oxides and zeolites using adsorbed probe molecules, Catal. Today 27 (1996) 377-401.

[8] S. Chen, A.M. Abdel-Mageed, C. Gauckler, S.E. Olesen, I. Chorkendorff, R.J. Behm, selective CO methanation on isostructural Ru nanocatalysts: the role of support effects, J. Catal. 373 (2019) 103-115.

[9] P.O. Scokart, P.G. Rouxhet, Characterization of the basicity of oxides through the infrared study of pyrrole adsorption, J. Chem. Soc. Faraday Trans 76 (1980) 1476-1489.

[10] M.A.A. Aziz, A.A. Jalil, S. Triwahyono, S.M. Sidik, Methanation of carbon dioxide on metal-promoted mesostructured silica nanoparticles, Appl. Catal. A 486 (2014) 115-122.

[11] T.J. Johnson, P.M. Aker, N.K. Scharko, S.D. Williams, Quantitative infrared and near-infrared gas-phase spectra for pyridine: absolute intensities and vibrational assignments, J. Quant. Spectrosc. Rad. 206 (2018) 355-366.

[12] M. Primet, P. Pichat, M. Mathieu, Infrared study of the surface of titanium dioxides. I. Hydroxyl groups, J. Phys. Chem. C 75 (1971) 1216-1220.

[13] E.P. Parry, An infrared study of pyridine adsorbed on acidic solids. Characterization of surface acidity, J. Catal. 2 (1963) 371-379.

[14] G. Busca, Spectroscopic characterization of the acid properties of metal oxide catalysts, Catal. Today 41 (1998) 191-206.

[15] M. Zaki, M. Hasan, A. Al-Sagheer, L. Pasupulety, In situ FTIR spectra of pyridine adsorbed on SiO_2-Al_2O_3, TiO_2, ZrO_2 and CeO_2: general considerations for the identification af acid sites on surfaces of finely divided metal oxides, Colloi. Surfaces A 190 (2001) 261-274.